6.1 Introduction

Growing global energy demand, scarcity of fossil fuel supply, and environmental concerns will increase the conventional energy crisis in the coming decades. That is why the establishment of energy storage infrastructure is urgently required to utilize the full potential of renewable energy sources in the fight against global warming and the depleting fossil fuel reserve (*191. Materials for Sustainable Energy*, n.d.). Portable electronic(Liang et al., 2019) [192], grid-scale energy storage(Whittingham, 1976b) [193], and Electric vehicles *(Goodenough & Braga, 2018b)* [194] need a safer, high voltage, and more economical energy storage system. So urgent need of material approaching the requirement. If looking for reliable energy storage infrastructure, Li-ion batteries(LiBs) are a good option with high gravimetric power density, energy density, and cyclic stability. Electric vehicles and portable electronic devices are in high demand and, electric vehicles are exerting pressure on existing lithium reserves. Very less lithium reserve on the earth and uneven global allocation make Li the future gold *(Tarascon, 2010b)*. In contrast to Li, sodium (Na) has ample natural resources that are evenly distributed throughout the world. Na, as a charge carrier, the second-lightest alkali metal in the periodic table, is also the fifth most prevalent element in the crust of the planet. Thus sodium-ion batteries (SIBs) emerge as good substitutes for Li because of properties like size (Na / 0.098 nm and Li / 0.069 nm), reduction potential vs. S.H.E (Li / -3.04V and Na / -2.7V), Cost(for carbonates of, Na / 0.07-0.37 €/kg and Li / 4.11-4.49 €/kg) *(James Abraham et al., 2021)*. Despite the Low gravimetric Energy density of Na(~1166mAh/g) compared to Li (~3862mAh/h), there are many additional challenges to the development of high capacity sodium-ion battery.

Different cathode chemistries based on oxide and polyanion have recently been

investigated because the cathode represents a significant amount of the cost of a battery overall *(Berthelot et al., 2011b; S. W. Kim et al., 2012; S. Kumar, Mondal, et al., 2022; Palomares et al., 2013; Pandey & Prakasha, n.d.)* Polyanion (PO_4^{3-}, SO_4^{2-}, $P_2O_7^{4-}$, BO_3^{3-}, SiO_4^{4-}) framework cathode material is of interest because of its large interstitial framework in which sodium-ion diffusion takes place. Sulfate framework-based cathodes give a high working potential by which high energy and power density batteries can be developed. An earlier report on Sulphate framework cathode $Na_2Fe(SO_4)_2.2H_2O$(70mAh/g vs. Na at C/20) *(Barpanda et al., 2014)* and $NaFe(SO_4)_2$ (80mAh/g vs. Na at C/10) *(Singh et al., 2015b)* have good capacity, but it is prone to moisture and lag behind the low theoretical capacity which can be encountered by the introduction of a phosphate group to the framework structure. $NaFe_2(SO_4)_2PO_4$ (100mAh/g vs. Na at C/10) *(Shiva et al., 2016b)*, $Na_3Fe_2(SO_4)_2PO_4$ (100mAh/g vs. Na at C/10) *(S. Kumar, Ranjeeth, et al., 2022b)*, $Na_3Fe_2(PO_4)_3$(100.8mA/g vs. Na at C/10) *(Cao et al., 2020)* and $Na_2V_2(PO_4)_3$ *(Du et al., 2013)*. In the current work, we are reporting a flake-like transition metal (Mo) oxypyrophosphate framework $Mo_2P_2O_{11}$ (MOP) for the reversible insertion of Na^+. The host MOP operates on Mo^{6+}/Mo^{4+} redox couple on sodium-ion insertion, and $Mo_2P_2O_{11}$ is known to give a specific capacity of 110 mAh/g in 2.3V-4.0 V for Lithium-ion *(B. Wen et al., 2013a)*.

6.2 Experimental Section

6.2.1 Materials Synthesis:

Since all of the compounds used for synthesis were of analytical quality, additional purification was not necessary. Synthesis of the precursor $MoO_2.HPO_4.H_2O$

followed the instructions in the literature *(Lister, Solellhavoup, et al., 2010; Lister, Rixom, et al., 2010a; B. Wen et al., 2013b)*. The schematic of the synthesis process is represented in Figure6.1 Initially, at about 180 °C, 15 g of MoO_3 (Alfa Aesar, 99.5%) was mixed in 45 mL of 88% phosphoric acid (Merk) on a magnetic stirrer at 500 r.p.m. next this solution was stirred for six hours or till green solution appeared then the solution was naturally cooled. 400 mL of 16 M HNO_3(Merk) was added to this solution, and it was now refluxed at 140 °C. Extra precautions should be followed because of working with concentrated acid. After the 12 hours of reflux reaction, an insoluble white precipitate($MoO_2.HPO_4.H_2O$) was obtained. Then precipitate is washed with acetone and deionized water, followed by drying at 100^oC in a hot air oven. To get the fine powder for better calcination, it is ground in an agate mortar pestle. Well-mixed and fine-grinded powder is calcined at 560^oC for 6 minutes in the muffle furnace at a heating rate of 20^o/hour. The final obtained blue powder is again well grinded to make it fine and carried out for further characterization.

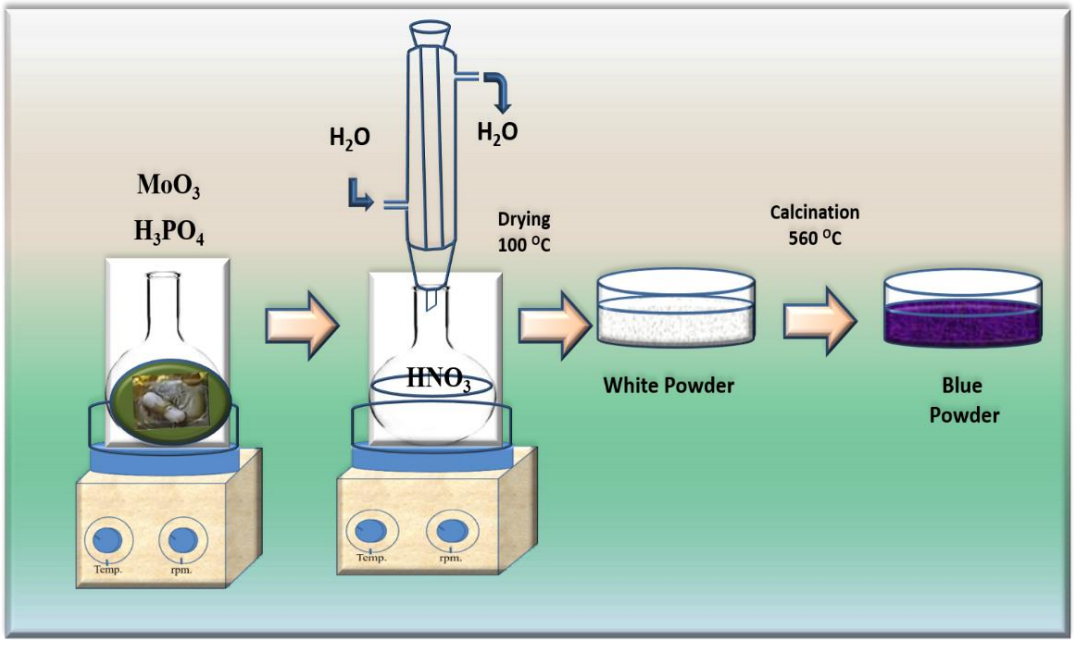

Figure 6.1. Synthesis Schematic of $Mo_2P_2O_{11}$.

Powder X-ray diffraction (Cu *K*α radiation, = 1.5418, the voltage of 40 kV; current= 30 mA, 2θ = 10º-50º) was used to evaluate the structural classification and crystallographic phase purity of the chemical in Bragg−Brentano reflection geometry. SEM was used to examine the surface morphology and particle size of MOP powder samples at a 20 kV accelerating voltage (FEI Quanta 650, FESEM); before the microscopy tests, the materials were dissolved in isopropanol, sonicated, and placed onto a carbon-coated Cu grid. Using a Bruker EDS system linked to the SEM apparatus, energy-dispersive X-ray (EDS) spectroscopy was used to confirm the composition and apparent homogeneity of the compounds. The chemical oxidation state of powder MOP is verified by X-ray photoelectron spectroscopy(XPS, *K* alpha Thermo Fischer Scientific). Thermal decomposition of synthesized powder is performed on TGA (TGA-50 Shimadzu Asia Pacific). The functional group present in the sample is analyzed by Fourier Transform Infrared Spectroscopy(FTIR, Thermofisher Scientific, USA). Electrochemical impedance spectra(EIS) is recorded in the frequency range of 0.1MHz to 0.01Hz at a voltage amplitude of 5mV. Impedance circuit fitting is done with the help of Z-Sim software.

6.3 Cell Assembling

For the electrochemical study, the working electrode composition $Mo_2P_2O_{11}$ (MOP) (active material), carbon black (Alfa Aesar), and Polytetrafluoroethylene (Alfa Aesar) were in the weight ratio of 65:25:10. The composite electrodes were flattened into a thin sheet, punched into circles with an average mass of 5-6 mg, and dried for 12 hours at 120 °C under vacuum. All the reporting electrochemical experiments were carried

out at 25 °C, room temperature. Galvanostatic charge/discharge cycling was conducted in coin cells with metallic Na (Aldrich) as the anode, PVDF-HFP polymer-coated Whatman glass fibre is used as a separator, and 10% FEC in propylene carbonate (PC, Aldrich) with 1 M $NaClO_4$ as electrolyte. At 25 °C, all coin cell fabrication was carried out in a glovebox (MBraun) with argon (H_2O: 0.1 ppm; O2: 0.1 ppm) present. The galvanostatic cycling was performed in the voltage range of 2.0-4.2 V (versus Na^+/Na). Na is intercalated and de-intercalated into the material and redox properties of the material were studied without further modification.

6.4 Results and Discussion

6.4.1 Structural Study

The powder x-ray diffraction (pXRD) pattern of the as-prepared powdered MOP is shown in Figure2 All the XRD diffraction peaks of $Mo_2P_2O_{11}$ are well matched and indexed to pnma space group of orthorhombic crystal structure (JCPDS card no. 15-0610). The average crystallite size (*D* in nm) is 32.19 nm calculated from the Debye sheerer formula as follows:

$$D = k\lambda / \beta \cos\theta$$

Where symbols used represent Debye sheerer constant (*k*, 0.9), the wavelength of incident X-ray (λ, 0.15406nm), FWHM (β, in radian) and peak position (θ, in radian). Material also shows that it is 87.55% crystalline and percentage Crystallinity of material is determined by the ratio of area of crystalline peak to the total area of plot (Amorphous and crystalline) using the origin 8.5 software. Further structure was refined by the Rietveld method using full-proof suite software. The observed XRD

pattern matched well with calculated diffraction intensities as seen in Figure 2. The structural parameter obtained from Rietveld refinement short description is shown in Table 6.1. The low *R*-value (R_{bragg} = 0.732%, R_f = 0.499%, and χ^2 = 4.2%) also suggests that the fitting of the refined structure is quite good.

The VESTA image in the inset of Figure 6.2 depicts that MoO_6 octahedra are connected with the PO_4 tetrahedra and form the 3-dimensional framework structure and thus form the large two-dimensional tunnel structure for Na^+ ion mobility. $Mo_2P_2O_{11}$ can be visualized as PO_4-$(Mo\text{-}O)_2$-O-PO_4.

Table 6.1. Structural refinement output Parameter of $Mo_2P_2O_{11}$

S.No.	Crystallographic parameter($Mo_2P_2O_{11}$)	Description
1.	Crystal System	Orthorhombic
2.	Space Group	pnma
3.	Unit Cell Volume	822.675 $Å^3$
4.	Lattice Parameter(a)	12.585231 Å
5.	Lattice Parameter(b)	6.300776 Å
6.	Lattice Parameter(c)	10.374634 Å
7.	R_p	6.0%
8.	R_{wp}	8.6%
9.	R_{exp}	4.1%
10.	χ^2	4.2%

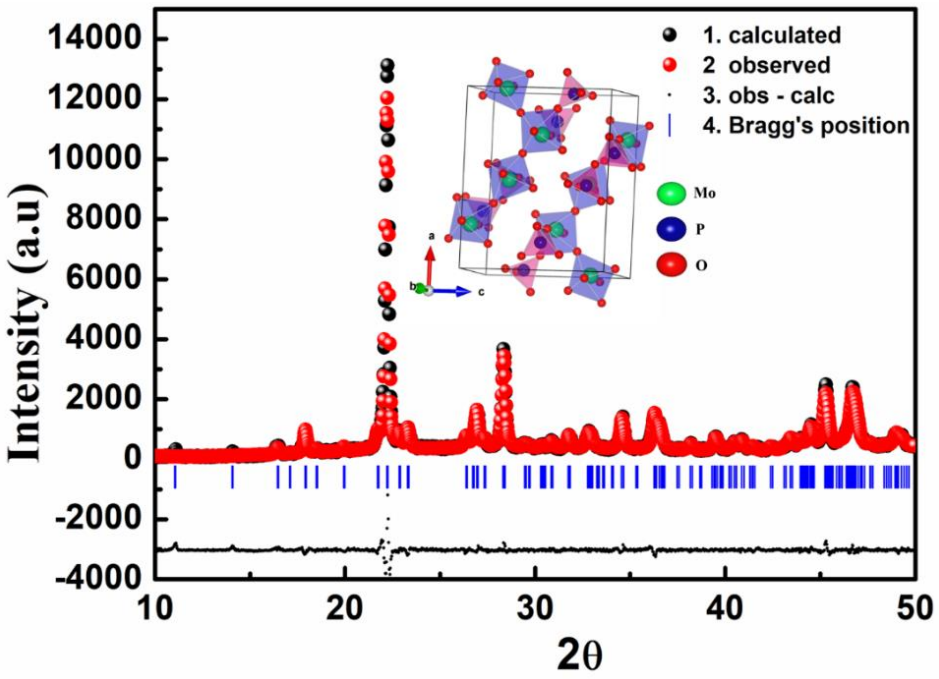

Figure 6.2 Rietveld refined powder X-ray diffraction pattern and VESTA image (in the inset) of $Mo_2P_2O_{11}$ (MOP).

Figure 6.3(a) shows the FTIR spectra in the wave number range of 3000-400cm^{-1}. P_2O_7 group can also be presented as O_3P-O-PO_3 that is why the vibrational frequency of PO_3 and P-O-P group can also be marked in the FT-IR spectra of the material. ν_{as} P-O denotes the asymmetric stretching frequency that arises at 1080cm^{-1} (990-1200cm^{-1}) due to the P-O bond vibration, whereas ν_{ss} P-O denotes the symmetric stretching frequency that arises at 936cm^{-1} (900-990cm^{-1}) for P-O bond in PO_4 or PO_3 group (M. Y. Wang et al., 2022; X. X. Zhao et al., 2020). ν_{ss} P-O-P at 737cm^{-1} denotes the symmetric stretching vibration of the P-O-P group of pyrophosphates and ν_b O-P-O represents the bending vibration frequency at 504cm^{-1} (500-680cm^{-1}) (Essehli et al., 2010; Kosova & Belotserkovsky, 2018; A. Kumar, Kumar, et al., 2022) the found resemblance of vibrational spectra explains the P-O environment in the as-prepared sample and confirms that the $Mo_2P_2O_{11}$ exists as PO_4-$(Mo\text{-}O)_2$-O-PO_4.

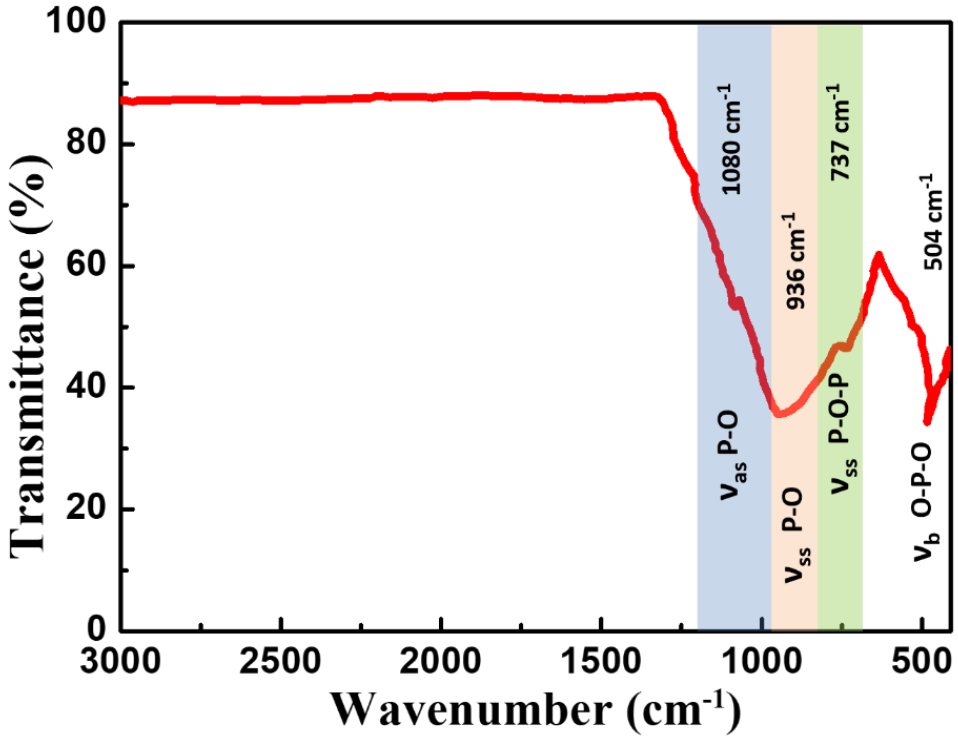

Figure 6.3 FT-IR spectra of $Mo_2P_2O_{11}$ powder recorded in the wavenumber range of 400-3000 cm^{-1}

The electronic state of Mo is confirmed by XPS and peaks are well-fitted with XPS peak 4.1 software as shown in Figure 6.4. Two peaks of Mo due to spin-orbit coupling, at a binding energy of 232.6 eV and 235.7 eV correspond to Mo $3d_{5/2}$ and $3d_{3/2}$, confirming the only one valance state (+6 oxidation state) of Mo in the sample (Vernickaitė et al., n.d.; C. Yang et al., 2020).

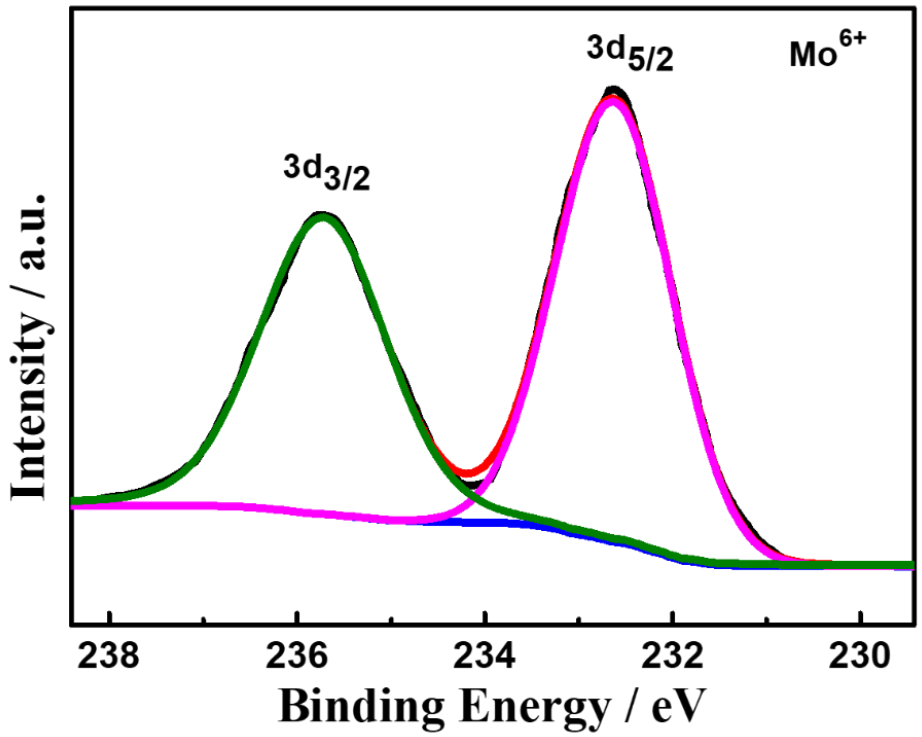

Figure 6.4 High resolution XPS spectra showing the presence of Mo^{6+} state in $Mo_2P_2O_{11}$.

Electronic transition and optical band gap property of the material is studied using the UV-VIS-DRS method in the wavelength range of 200-900 nm (Figure 6.5). It is convenient to measure the optical properties by UV-VIS-DRS method, but for band gap calculation, reflectance or transmittance spectra cannot be used directly because of the low intensity of Eg transition. Diffuse reflectance spectra are transformed into the Kebulka -Munk function F(R) vs. wavelength. Spectra recorded in diffuse reflectance (*R*) transformed to absorption coefficient *K* and scattering coefficient *S* as per Kubelka Munk model.

$$\frac{K}{S} = \frac{(1-R)\text{^}2}{2R} \equiv F(R) \qquad \text{Eq. 2.7}$$

Tauc plot,

$$(\alpha h\nu)^{1/n} = A\,(h\nu - E_g) \qquad \text{Eq. 2.8}$$

is transformed by replacing absorption coefficient α with the Kubelka Munk function *F(R)* as

$$(F(R)h\nu)^{1/n} = A\,(h\nu - E_g) \qquad \text{Eq. 2.9}$$

Where h = planks constant, *v* frequency of light, A is Absorbance, E_g is band gap of material and n = 1/2 (direct allowed transition), 2 (indirect allowed transition) (*219. Pr3+ Doped BaNb2O6 Reddish Orange Emitting Phosphor for Solid State Lighting and Optical Thermometry Applications _ Elsevier Enhanced Reader*, n.d.). The absorption band for polyanionic compound $Mo_2P_2O_{11}$ obtained at 615nm is due to the ligand-to-metal charge transfer. The optical band gap was calculated from a Tauc plot of $(F(R)h\nu)^2$ vs. photon energy (*hν), the* best fit is observed for direct allowed transition, and obtained band gap is 2.0 eV.

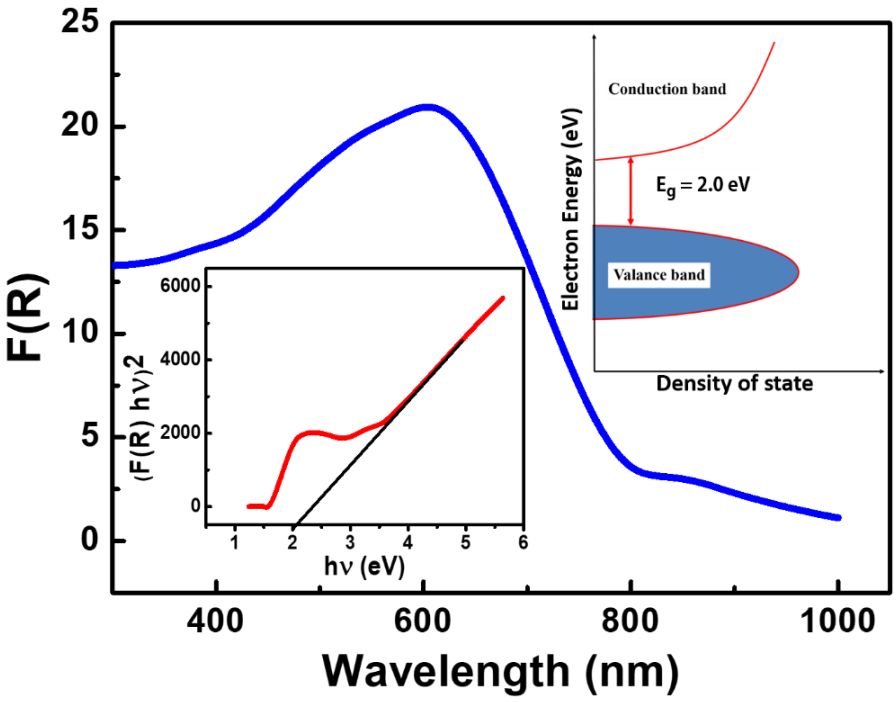

Figure 6.5 UV-Vis. spectroscopy from 200-900 nm, and inset shows the optical band gap of material.

TGA is a thermal technique that is frequently utilized in all stages of research, quality assurance, and manufacturing processes. When the material is heated in a controlled environment, it monitors changes in mass as a function of temperature. Figure 6.6 represents the Thermal stability and phase change monitoring of MOP using TGA and it was observed that in a horizontal line from room temperature to 300^{o}C, there is no weight indicating the material is thermally stable. From 300^{o}C to 725^{o}C, there is a small, steady loss (0.6wt%) corresponding to the removal of crystallized water to the structure and formation of MOP. There is a significant weight loss (around 14.8%) between 725^{o}C and 800^{o}C, which is caused by phosphate decomposition(Lister, Rixom, et al., 2010b) and higher thermal stability of MOP up to 725^{o}C.

$$Mo_2P_2O_{11} \xrightarrow{T > 725^{o}C} Mo_2P_2O_8 + 3/2\ O_2(g)$$

Eq. 6.1

Since attachment of $P_2O_7^{4-}$ group to the M-O bond makes it less covalent and shifts its decomposition temperature to a higher temperature range, thus, ionic nature of $P_2O_7^{4-}$ provides pyrophosphate more stable than the phosphate or sulphate and makes it highly thermally stable.

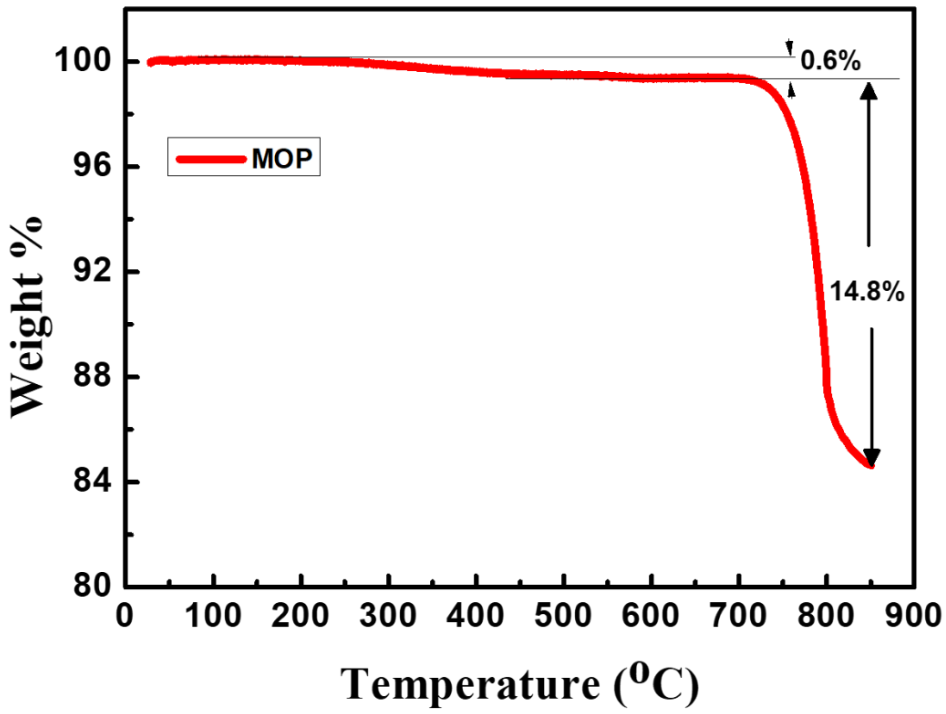

Figure 6.6 Thermogravimetric Analysis profile in temperature range of RT to 850°C.

SEM image of MOP shows agglomerated flake morphology (Figure 6.7(a)), flakes are randomly oriented and its size distribution histogram is shown in the inset and has a mean flake size of 0.45µm calculated using ImageJ software. In a high-resolution SEM image (Figure 6.7(b)), MOP flakes are homogeneously distributed and randomly oriented to form a hollow network which helps in better electrolyte penetration and Na^+ ion migration. The EDS study (Figure 6.7(c)) also confirms the elemental presence (Mo, P, O) in the MOP composition of the material, as the EDS composition of elements and theoretical composition is almost the same. The electrode is prepared using the well mixing of conducting carbon and active material with the binder in an agate mortar pestle for two continuous hours in NMP. Carbon mixing with the active material enhances the electronic conductivity of the material to facilitate better electron transfer during charging-discharging of MOP as well as inhibit the particle

agglomeration (particle size of electrode, 0.056 µm as compared to MOP powder,0.45µm) can be seen in SEM image of the as-prepared electrode (Figure 6.8(a)).

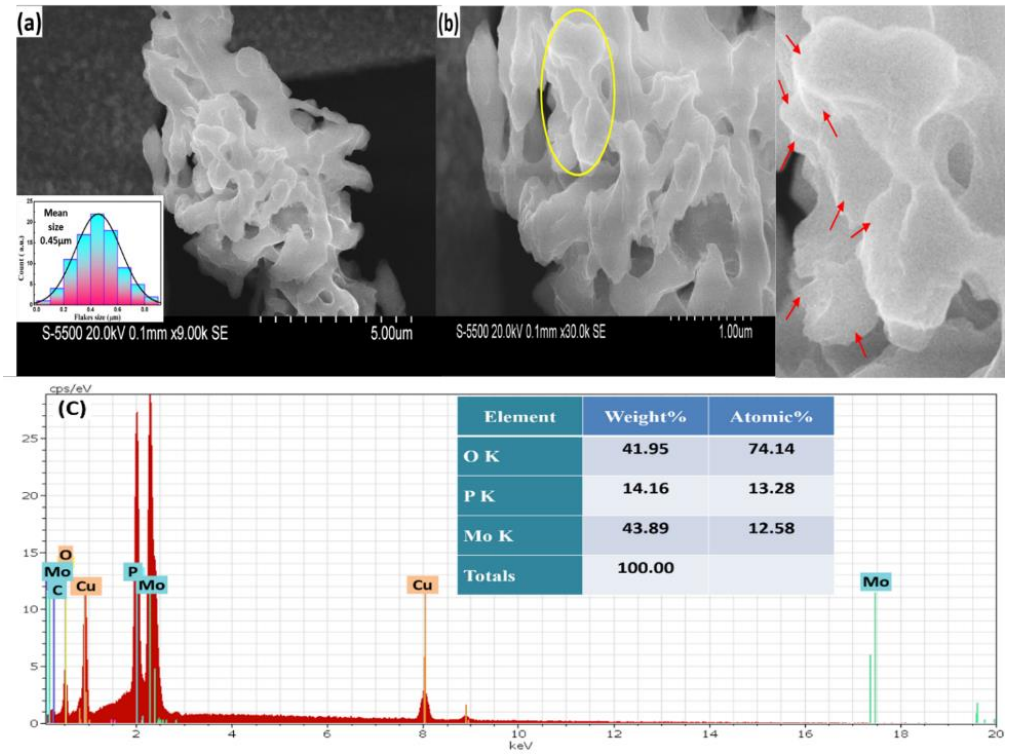

Figure 6.7 (a) SEM image of as-prepared powdered MOP sample. **(b)** High magnification image showing flakes. **(c)** EDS image showing the elemental composition.

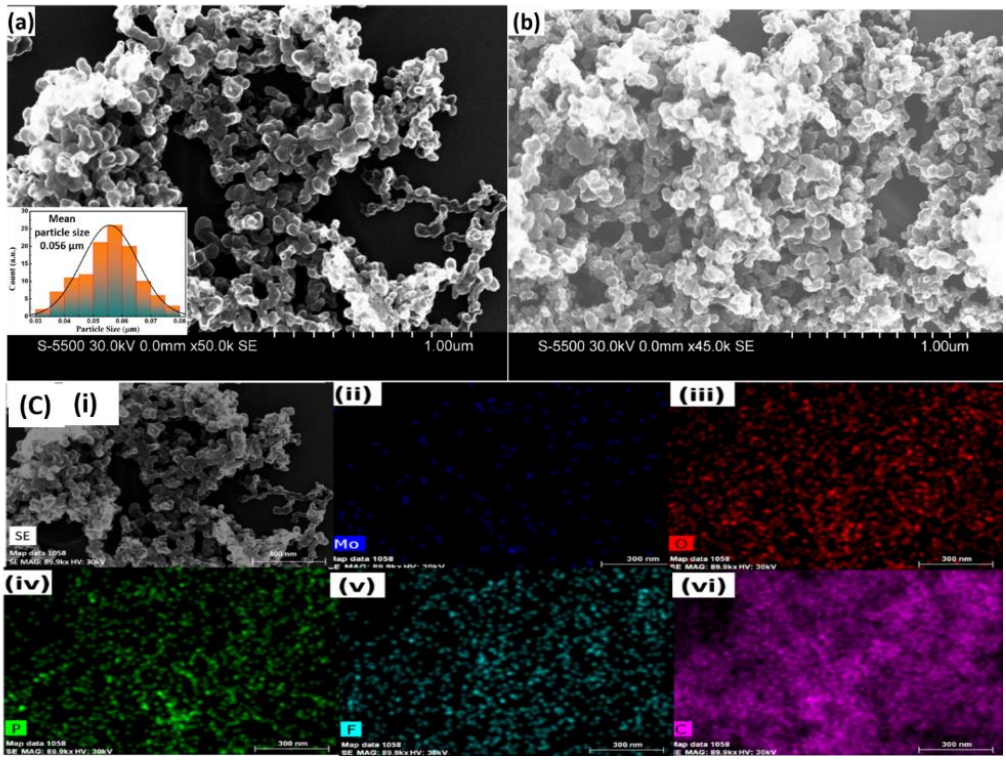

Figure 6.8 SEM image of as-prepared $Mo_2P_2O_{11}$ electrode **(a)** before cycling **(b)** after cycling **(c)** (i) selected area for elemental mapping and elemental distribution of (ii) Molybdenum (iii) Oxygen (iv) phosphorous (v) fluorine (vi) carbon in the sample.

The material also shows stable morphological stability after the 100 cycles of charge-discharge and the morphology of the electrode appears nearly the same after the cycling (figure 6.8(b)). Elements (Mo, O, P, F, C) are homogeneously distributed throughout the area in the as-prepared electrode, as shown in the elemental mapping (Figure 6.8(c)).

6.4.2 Electrochemical Study

To learn more about the electrochemical characteristics of MOP electrodes, a galvanostatic charge-discharge cycling experiment and cyclic voltammetry were carried out. Figure 6.9(a) shows the first 20 cycles of the cyclic voltammograms for

the MOP electrodes that exhibit a potential plateau at 2.75 ad 3.2 V during the first discharge cycle, which can be assigned to the formation of $Na_{1+x}MoP_2O_{11}$. During the 1st charge, the cycle peak at 3.0 and 3.25 V can be assigned to the de-intercalation reaction. From the 2nd cycle onwards, the peaks are shifted towards lower potential, and a decrease in peak current was observed. However, differences in cathodic and anodic current remain almost the same. This means intercalation is reversible. The strong intense electrochemical reversibility of the system is indicated by peaks in subsequent cycles of MOP. The intercalation/de-intercalation reaction is depicted in eq.6.2

$$Mo_2P_2O_{11} + yNa^+ + ye^- \underset{\text{Charge}}{\overset{\text{Discharge}}{\rightleftharpoons}} Na_yMo^{6+}_{2-x}Mo^{4+}_{x}P_2O_{11} \qquad \text{Eq.6.2}$$

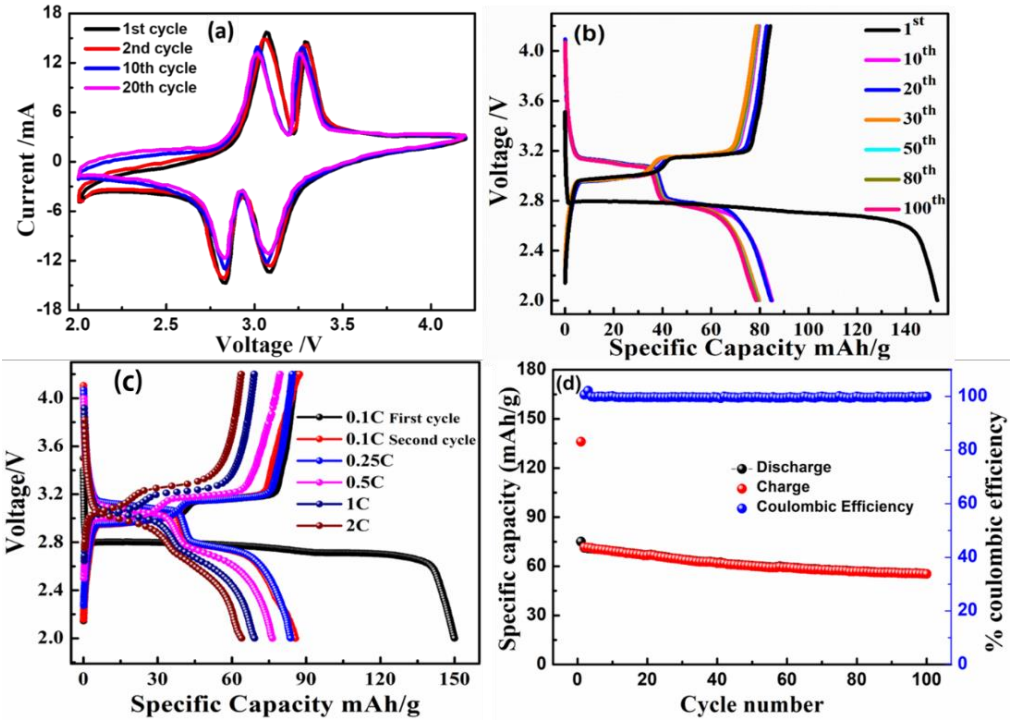

Figure 6.9 Electrochemical analysis of MOP **(a)** Cyclic voltammogram of MOP for first 20 cycles at a scan rate of 0.2mV/s (b) selected charge-discharge profile of MOP (1st, 10th, 20th, 30th, 50th, 80th, and 100th cycle) at C/10 current rate. (c) Capacity vs. voltage plot of MOP at different C rates (0.1C, 0.25C, 0.5C, 1C, 2C) (d) Capacity retention and coulombic efficiency of MOP as a function of Cycle number at 2C.

Figure 6.9(b) shows the galvanostatic charge-discharge voltage profiles of MOP electrodes for cycles 1, 10, 20, 30, 50, 80 and 100 at 0.1 C-rate. In the first discharge cycle, voltage plateau is observed at 3.2 and 2.75 V versus Na/Na^+ cell. The electrochemical performance of MOP is monitored on Na-ion cells at the current rate of C/10. The obtained cell reaction voltage is 3.0 V of MOP as compared to 2.2 V for MoO_3 for 1^{st} Na^+ ion intercalation and is due to the inductive effect of the phosphate group (*221. MoO3 Voltage*, n.d.). In the very first discharge cycle, the discharge capacity reaches 152 mA/g which corresponds to 2.4 Na ion insertion per formula unit. Theoretical capacity of $Mo_2P_2O_{11}$ for per sodium insertion/de-insertion is 62 mAh/g and for two sodium insertion/de-insertion it is 124 mAh/g as calculated using equations 2-4. Here we observed capacity of ~90mAh/g i.e., reversibly intercalating 1.5 Na after first cycle means average charge on Mo is due to charge ordering of Mo^{6+} and Mo^{4+}. This difference in the experimental and theoretical capacity arises due to the irreversible structural changes (orthorhombic to monoclinic) and SEI formation after the first cycle which limits to achieve the theoretical capacity. Here observed charge-discharge plateaus are in good agreement with the *CV* plot. During an initial discharge (insertion) and charge (extraction) capacities for the MOP electrode were 152 and 89 mAh/g respectively, such a capacity difference in charge and discharge cycle is probably due to material activation also related to stable SEI formation over the electrode. With Coulombic efficiency of 99.3% at 0.1C (calculated as per equation 6.3), the discharge and charge capacities of 88.3 and 88.9 mAh/g were attained after the first cycle. With a Coulombic efficiency, a high reversible discharge capacity of 79.6 mAh/g is attained in the 100th cycle. (*CE*) of ~ 100%. Even though the electrochemical energy storage

capacity of $Mo_2P_2O_{11}$ is close to 80 mAh/g, it is near ~1.3 Na intercalation per formula structure to the $Mo_2P_2O_{11}$ after 100cycle.

$$CE = \frac{\text{Discharge capacity}}{\text{Charge Capacity}} * 100 \quad \text{mAh/g} \qquad \text{Eq. 6.3}$$

$$\text{Theoretical capacity } (C_{th}) = nF / (M\text{w} * 3.6) \qquad \text{Eq. 6.4}$$

$$\text{Fraction intercalation or deintercalation} = \frac{\textbf{Discharge or Charge capacity}}{\textbf{Theoritical capacity}} \qquad \text{Eq. 6.5}$$

Where n is the number of electrons participating in the redox process, F is Faraday constant 96485 and M_w is the molecular weight of active material

To study the cyclability at varying currents against Na, MOP was cycled in a half-cell configuration in the potential range 2.0-4.2 V. Recovery performance of MOP is performed at different current rates (0.1 C, 0.25C, 0.5C, 1C, and 2C) to examine its rate capability Figure 6.9(c). The stable cyclability arises from a combination of factors related to the stable framework structure of MOP. The first discharge capacity at *0.1C first cycle* shows a specific capacity of ~150 mAh/g and *0.1C second cycle* it shows a capacity of ~90 mAh/g it is due to the irreversible structural changes taking place as well as SEI formation at first cycle due to the sodium insertion, as seen in the XRD pattern of after charge-discharge in the later plot of fig 6.11. The specific discharge capacities were found to be 88, 85, 76, 69, and 63 mAh/g, respectively, under a drastic change in current rates (0.1, 0.25, 0.5, 1, and 2 C). After some cycles of sodium insertion and de-insertion, it can be understood that reversible intercalation becomes easier in the host lattice as seen in plot of cycle number vs. specific capacity and coulombic efficiency in Figure 6.9(d), as it retains coulombic efficiency of ~100% after 100 cycles.

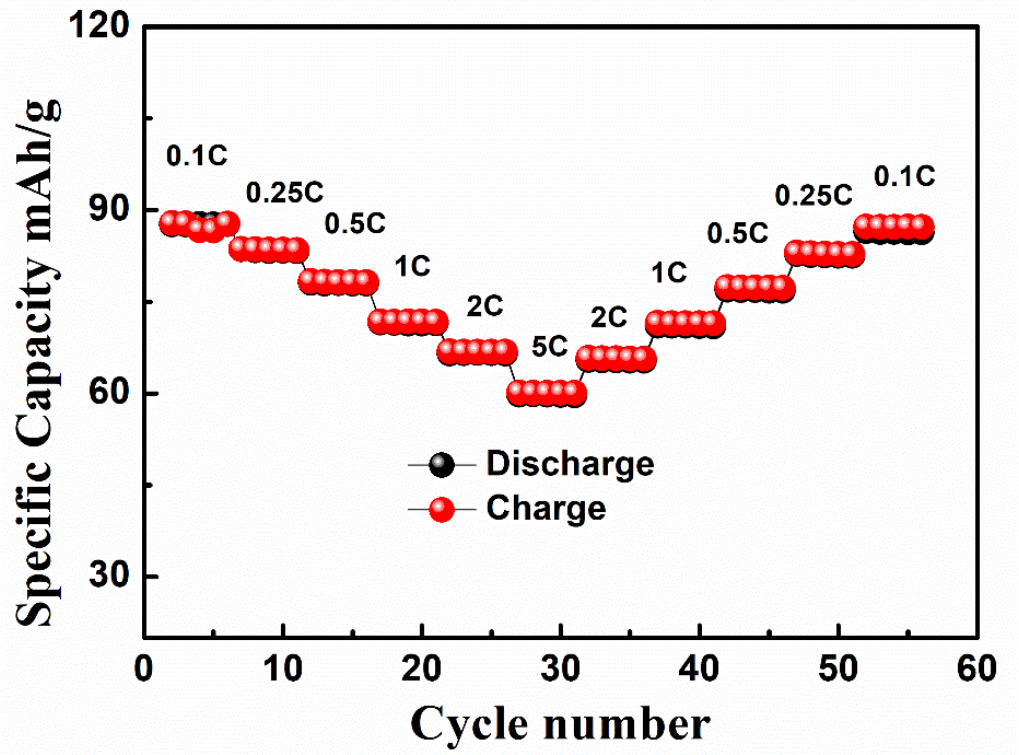

Figure 6.10 Stability performance of MOP at different C-rate.

Recovery performance of material is examined by performance of material under the varying current rates (0.1, 0.25, 0.5, 1, 2, 5 C) (Figure 6.10). The observed capacities are 88(0.1C), 85(0.25C), 76(0.5C), 69(1C), and 63(2C) and 58(5C) mAh/g i.e., Found to be recovery of initial capacity values. Upon returning the testing current to its starting low C-rate (= 0.1 C), the capacity is approached nearly to the initial value again; this shows there is no electrolyte degradation or active material loss and shown by capacity at varying current load. The enhanced rate capability of the MOP is attributed to its stable open framework structure. Charge discharge plot at different current density tells that even heavy applied current density, MOP shows a good recovery performance. A greater electrode-electrolyte contact area is ensured as a result of the ball-milled MOP's improved mechanical stability, which further improves electron and sodium-ion transport (Fang et al., 2019; Q. Liu et al., 2021; Niu et al., 2022). Charge discharge

specific capacity of different cathode materials have been detailed studied and tabulated in Table 2 (*229. MoP2O7 Cathode for Sodium-Ion Battery*, n.d.; Barpanda, Liu, et al., 2013b; Barpanda, Lu, et al., 2013; Barpanda, Ye, et al., 2013; W. Deng et al., 2018; Drozhzhin et al., 2019).

Table 6.2: Comparision of Current work $Mo_2P_2O_{11}$

S. No.	Materials	C-Rate	Capacity	Voltage	Anode	References
1.	$Na_2FeP_2O_7$	C/10	90mAh/g	3.0V	Na	(Barpanda, Liu, et al., 2013b)
2.	$\beta Na_2MnP_2O_7$	C/20	80mAh/g	3.6V	Na	(Barpanda, Ye, et al., 2013)
3.	βNVP_2O_7	C/10	104mAh/g	3.9V	Na	(Drozhzhin et al., 2019)
4.	$Na_2CoP_2O_7$	C/20	80mAh/g	3.0V	Na	(Barpanda, Lu, et al., 2013)
5.	MoP_2O_7	C/10	95mAh/g	2.0V	Na	(*229. MoP2O7 Cathode for Sodium Ion Battery*, n.d.)
6.	Layer-$Mo_2P_2O_{11}$	C/10	68mAh/g	2.8V	Na	(W. Deng et al., 2018)
7.	Flake-$Mo_2P_2O_{11}$	C/10	89mAh/g	3.0V	Na	Current work

Exploring structural changes during chemical and electrochemical Sodiation will assist in understanding the structural stability of the material (Ge et al., 2015) (Figure 6.11). After dismantling the discharged coin cells in a glovebox, we further examined the electrochemically sodiated phases of $Mo_2P_2O_{11}$ at various levels of charge and discharge. On first discharge, there is 2.5 Na sodium insertion into the structure and, there is an irrereversible change in the XRD pattern observed (*235. A Mixed-Valence Molybdenum Monophosphate with a Three-Dimensional Framework_ LiMo2O3(PO4)2 _ Elsevier Enhanced Reader*, n.d.; Feng et al., 2019; Ledain et al., 1996; C. J. Pan et al., 2018). On the second cycle onward charge-discharge pattern is well matched with JCPDS card no. 01-074-1387. Here first, Na insertion distorts angle β from 90^o to $91.19^{o,}$ and thus crystal system changes to a monoclinic P21/n space group. On further charging and discharging, there is smooth and structurally stable electrochemical processes that enhance the reversible electrochemical performance of the electrode. Structural study of the electrode after first discharge (chemical sodiation of $Mo_2P_2O_{11}$) results in no change in the lattice parameter on 1.5 sodium-ions insertion and deinsertion reversibly in the host lattice $Mo_2P_2O_{11}$ (L. Yang et al., 2019).

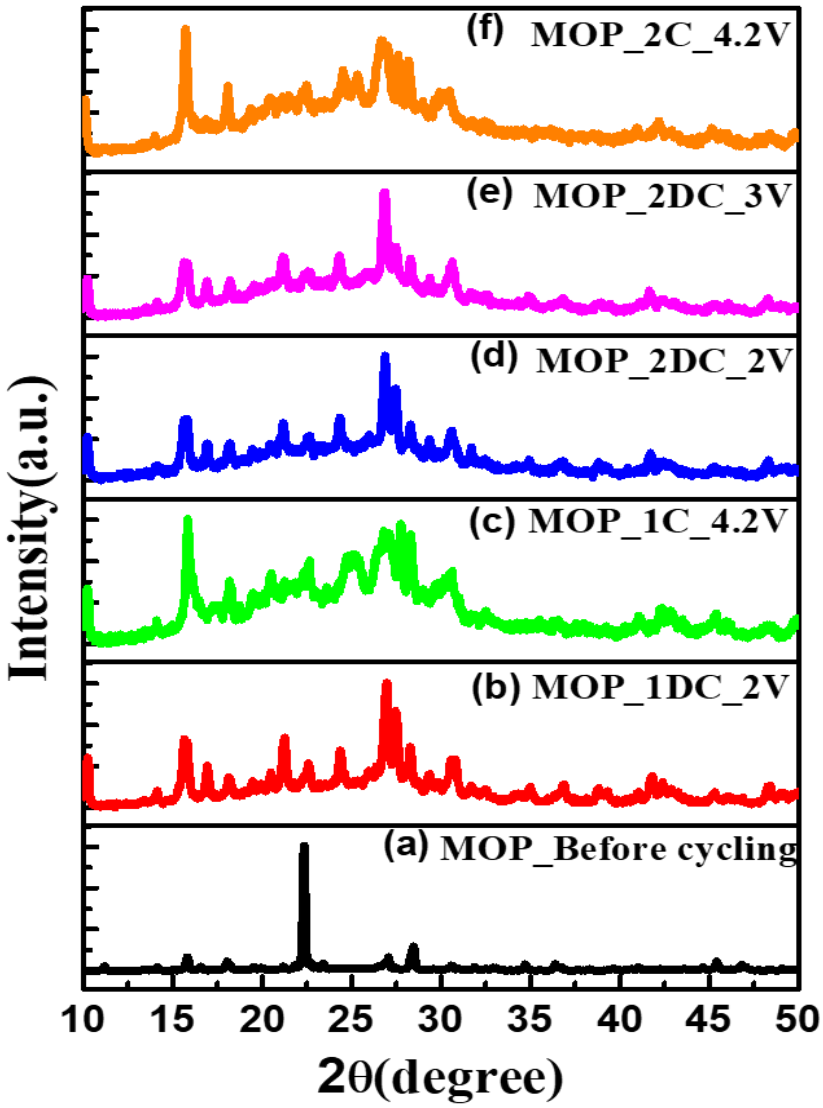

Figure 6.11 Ex-situ XRD for MOP cycled between 2.0 V and 4.2 V at a current density of 0.1 C vs. Na^+ /Na.

EIS is performed to investigate the electronic conductivity and improve the ion diffusion coefficient to enhance the charge transfer process taken at 25% SoC. As seen in EIS spectra (Figure 6.12(a)) is composed of solution resistance (*R*s), 27.4Ω at a higher frequency followed by two semicircle first circle arise at a higher frequency is due to the formation of solid electrolyte interface($R_{SEI,}$) 153.2 Ω and second semicircle at lower frequency is due to the charge transfer resistance (*R*ct), 406 Ω from solution to

the electrode surface. At lower frequencies, sodium-ion diffusion into the solid phase (Y. Chen et al., 2022; B. Shen et al., 2018) gives rise to the slope that is attributed to Warburg impedance. Sodium-ion diffusion coefficient (D_{Na}) is calculated using the following formula,

$$D_{Na} = \frac{R^2\ T^2}{2(n^2\ F^2\ )^2\ A^2\ C^2\ \sigma w^2} \qquad \text{Eq. 2.12}$$

Where R is gas constant (8.314 J mol^{-1} K^{-1}), T is the temperature in kelvin (300 K), n is the number of electron transfers during the redox process, F is faraday constant (96485 C mol^{-1}), A is the electrode surface area (0.5 cm^2), C is sodium-ion concentration in the electrolyte (1 M), σ_w (Warburg coefficient, 46.75) is the slope obtained from linear fitting of Z' (real part of impedance) and $\omega^{-0.5}$ (angular frequency) (Figure 6.12(b)) as following;

$$Z' = R_S + R_{ct} + \sigma_w\, \omega^{-0.5} \qquad \text{Eq. 2.13}$$

Where R_s is electrolyte resistance, R_{ct} is charge transfer resistance. Thus, the calculated diffusion of Na ion (D_{Na}) as per equations (5) and (6) is 0.7 x 10^{-16} cm^2s^{-1}. Due to the discharge state, sodium layer spacing is low and experiences low diffusion kinetics. Further, with improved surface nano engineering, better kinetics and capacity can be obtained (Cook et al., 2017; L. Yang et al., 2018).

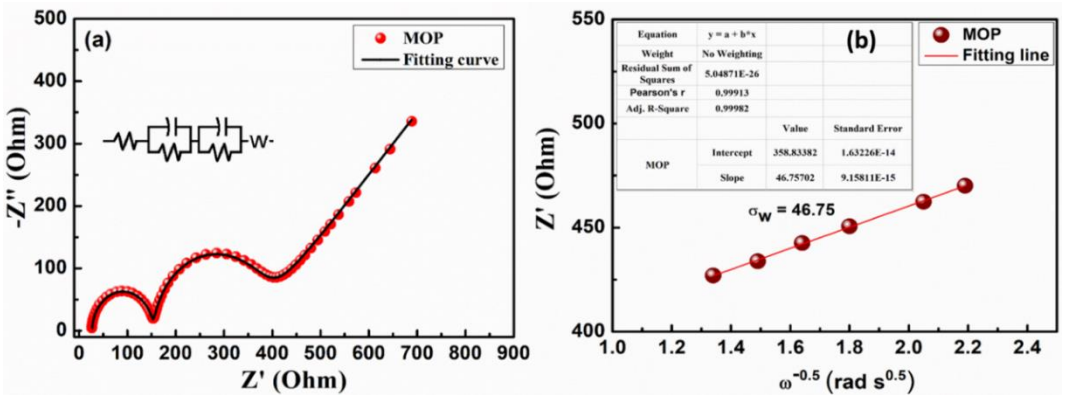

Figure 6.12. **(a)** Nyquist plot of MOP with fitting curve **(b)** correlation between Z_{real} (Z') and $\omega^{-0.5}$

6.5 Concluding Remark:

- New polyanionic framework (P_2O_7) type material with Mo has better phase stability than NFS.

- Synthesis of $Mo_2P_2O_{11}$ an orthorhombic structure, pnma space group in the staked flakes-like morphology. The structure contains corner-sharing of octahedra of Mo with a PO_4 tetrahedron and makes a tunnel-like structure for an easy Na ion migration path.

- ~1.4 Na can be reversibly intercalated and deintercalated into the $Mo_2P_2O_{11}$ framework.

- initial discharge capacity of ~90 mAh/g at C/10 current rate or specific energy of 270Wh/kg and it is 63mAh/g after 100 cycles

- intercalation/deintercalation of 1.4Na ion per mol of MOP with coulombic efficiency ~100%.

- Better capacity retention from 2^{nd} to 100 cycles. (5 mAh/g capacity loss in MOP as compared to 12mAh/g capacity loss in NFPS)

- There is a significant 0.8 Å expansion in the '*a'* lattice after the first cycle sodiation (2.4 Na per molecule of MOP), as evident in the charge-discharge plot and powder XRD plot of sodiated MOP.

- With stable electrochemical performance coupled with high coulombic efficiency, $Mo_2P_2O_{11}$ is presented here as a potential cathode material for sodium-ion batteries.

- SEI impart a big role in ion diffusion and decreases ion diffusion to 0.7×10^{-16} cm^2s^{-1}

- Further nanoengineering can improve the performance of the electrode by improving the active surface area of the electrode. This work opens the interest of researchers to explore more framework materials to develop superior electrodes for Na-ion batteries.